

## **Communications**





How to cite: Angew. Chem. Int. Ed. 2023, 62, e202305251 doi.org/10.1002/anie.202305251

# Solar-Driven CO<sub>2</sub> Conversion via Optimized Photothermal Catalysis in a Lotus Pod Structure

Hongmin Wang, Shuting Fu, Bo Shang, Sungho Jeon, Yiren Zhong, Nia J. Harmon, Chungseok Choi, Eric A. Stach, and Hailiang Wang\*

Abstract: Photothermal CO2 reduction is one of the most promising routes to efficiently utilize solar energy for fuel production at high rates. However, this reaction is currently limited by underdeveloped catalysts with low photothermal conversion efficiency, insufficient exposure of active sites, low active material loading, and high material cost. Herein, we report a potassiummodified carbon-supported cobalt (K+-Co-C) catalyst mimicking the structure of a lotus pod that addresses these challenges. As a result of the designed lotus-pod structure which features an efficient photothermal C substrate with hierarchical pores, an intimate Co/C interface with covalent bonding, and exposed Co catalytic sites with optimized CO binding strength, the K+-Co-C catalyst shows a record-high photothermal  $CO_2$  hydrogenation rate of 758 mmol  $g_{cat}^{-1}h^{-1}$  $(2871 \text{ mmol g}_{\text{Co}}^{-1} \text{h}^{-1})$  with a 99.8% selectivity for CO, three orders of magnitude higher than typical photochemical CO2 reduction reactions. We further demonstrate with this catalyst effective CO<sub>2</sub> conversion under natural sunlight one hour before sunset during the winter season, putting forward an important step towards practical solar fuel production.

Utilizing sunlight to drive CO<sub>2</sub> reduction reactions has the potential for storing solar energy in chemical fuels and mitigating climate change caused by increasing CO2 emissions.<sup>[1]</sup> Photochemical reactions, which utilize semiconductors/chromophores and co-catalysts to transfer electrons from reducing reagents to CO<sub>2</sub> upon photoexcitation, are a prevalent method for solar-driven CO<sub>2</sub> reduction.<sup>[2]</sup> However, this method utilizes only a fraction of the UV and visible part of the solar spectrum, which together accounts for 48% of the total energy, and typically shows low

production rates at the µmol g<sub>cat</sub> -1 h<sup>-1</sup> scale. [3-6] Moreover, most photochemical CO2 reduction reactions require sacrificial electron donors to facilitate thermodynamics and suppress undesired back electron transfer, which considerably increases the cost. [7] Photothermal CO<sub>2</sub> reduction can make use of the full solar spectrum and reach production rates in the range of mmolg<sub>cat</sub><sup>-1</sup>h<sup>-1</sup>, three orders of magnitude higher than photochemical reactions. [8-9] The high temperature condition directly driven by solar irradiation can enable endothermic reactions between CO2 and a reducing agent such as H<sub>2</sub>, CH<sub>4</sub>, or H<sub>2</sub>O. [10]

Photothermal CO<sub>2</sub> hydrogenation converts CO<sub>2</sub> to CO or syngas (CO<sub>2</sub>+H<sub>2</sub>→CO+H<sub>2</sub>O), which are main feedstocks for industrial reactions such as the Fischer-Tropsch and Monsanto/Cativa processes.[11,12] However, photothermal catalysts for this reaction are still underdeveloped, limited by low photothermal conversion efficiency and insufficient exposure of active sites. [8] Most of these catalysts are catalytically active nanoparticles dispersed on high-production rates based on the active material. This value drops to  $10^1 \, \text{mmol} \, g_{\text{cat}}^{-1} \, h^{-1}$  when normalized to the total catalyst mass (including the support) because of the low active material mass loading. [20] Utilizing low-density carbon materials as supports can increase active mass loading up to 90 wt.% and improve overall CO productivity to 132 mmol g<sub>cat</sub><sup>-1</sup>h<sup>-1</sup>, but active material-based productivity falls below 150 mmol gactive 1 h-1 possibly due to carbon covering active sites.<sup>[21]</sup>

In this work, we developed a potassium-modified carbon-supported cobalt (K+-Co-C) catalyst with a lotuspod structure for efficient photothermal CO<sub>2</sub> hydrogenation (Figure 1a). We utilize the strong coordination interaction between Co<sup>2+</sup> ions and the hydroxyl groups of natural cotton[22] to create an intimate interface between highly dispersed Co nanoparticles and the carbon photothermal support after pyrolysis. Subsequent modification with K<sup>+</sup> protects the Co sites from CO poisoning and prevents CO methanation. Further H<sub>2</sub> treatment creates a lotus-pod-like structure exposing the Co nanoparticles embedded in the hierarchical porous carbon support. For photothermal CO2 hydrogenation (1:1 H<sub>2</sub>/CO<sub>2</sub> by volume) in a flow reactor under 2.8 W cm<sup>-2</sup> Xe lamp illumination and ambient pressure, our K<sup>+</sup>-Co-C catalyst shows highly selective (99.8%) CO production at a stable rate of  $758 \text{ mmol g}_{cat}^{-1} \text{ h}^{-1}$  $(2871 \text{ mmol } g_{Co}^{-1} h^{-1})$ , which is 4 times higher than the previous record. [15] In a batch reactor, the catalyst shows

Department of Chemistry, Yale University

CT 06520 New Haven, (USA)

E-mail: hailiang.wang@yale.edu H. Wang, S. Fu, B. Shang, Y. Zhong, N. J. Harmon, C. Choi, H. Wang

Energy Sciences Institute, Yale University CT 06516 West Haven, (USA)

S. Jeon, E. A. Stach

Department of Materials Science and Engineering, University of Pennsylvania

PA 19104 Philadelphia, (USA)

<sup>[\*]</sup> H. Wang, S. Fu, B. Shang, Y. Zhong, N. J. Harmon, C. Choi, H. Wang

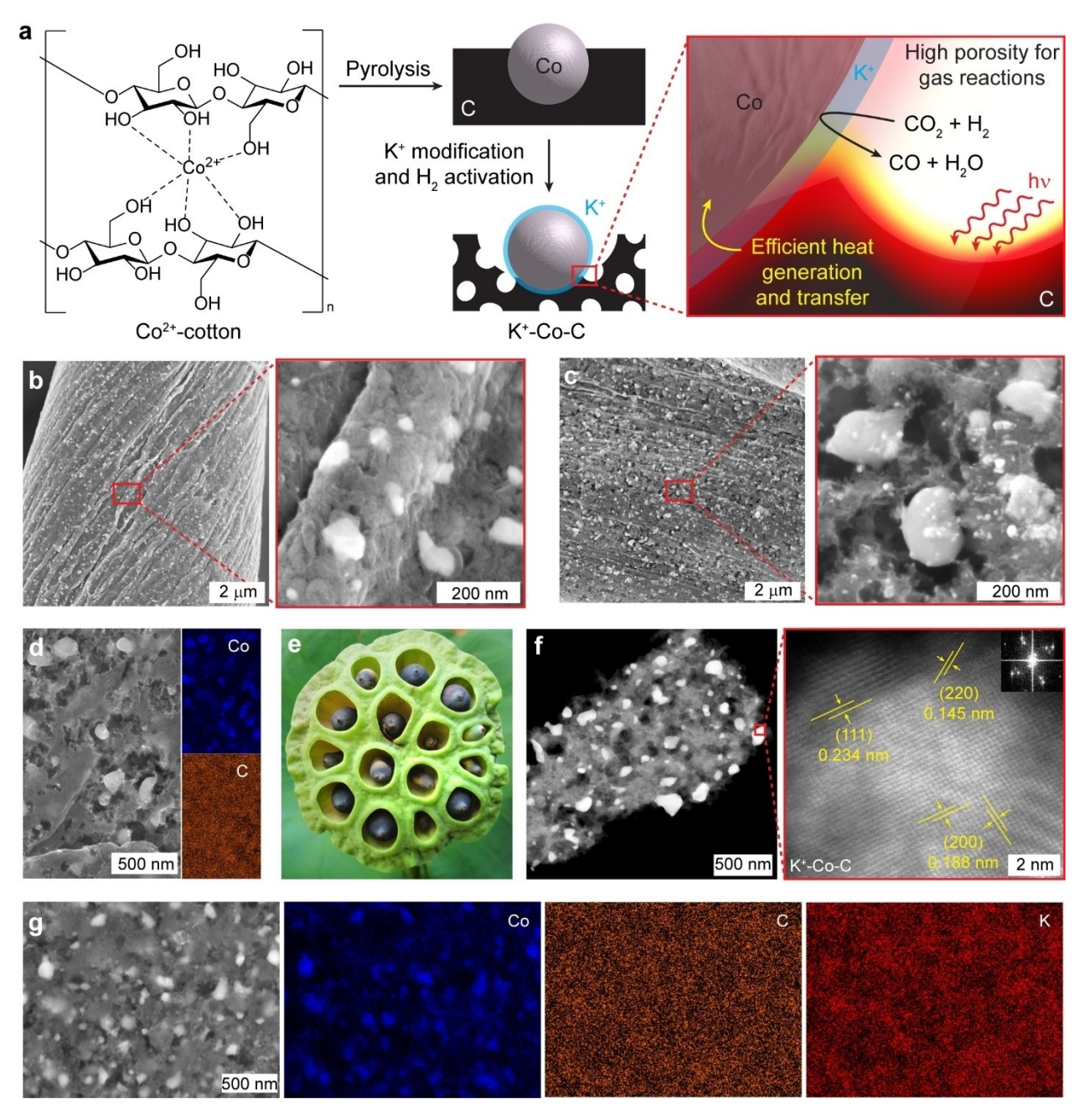


Figure 1. Synthesis, structure, and photothermal response of Co–C catalysts. a) Synthetic route for  $K^+$ –Co–C catalyst with desirable structure and properties for photothermal  $CO_2$  hydrogenation. b) SEM images of as-pyrolyzed Co–C. c) SEM images and d) EDX maps of  $H_2$ -activated Co–C. e) Photograph of a lotus pod. Credit: tanakawho (https://www.flickr.com/photos/28481088@N00/3908915225). f) HAADF-STEM images and g) EDX maps of  $H_2$ -activated  $K^+$ –Co–C.

>95 % CO selectivity with CO<sub>2</sub> conversion close to the thermodynamic equilibrium value.

The carbon-supported cobalt (Co–C) catalyst was synthesized by soaking a natural cotton pad in an aqueous Co(NO<sub>3</sub>)<sub>2</sub> solution and pyrolyzing the impregnated substrate in Ar at 900°C. The powder X-ray diffraction (XRD) pattern of as-pyrolyzed Co–C shows peaks corresponding to graphite and cobalt metal (Figure S1), suggesting that our synthesis successfully graphitizes the cotton and reduces Co<sup>2+</sup> to Co(0). Scanning electron microscopy (SEM) charac-

terizes the material structure as  $\approx 100\,\mathrm{nm}$  nanoparticles embedded in a matrix (Figure 1b). The Co particle size remains the same when elevating the pyrolysis temperature to  $1000\,^\circ\mathrm{C}$ , decreases to  $\approx 30\,\mathrm{nm}$  at  $700\,^\circ\mathrm{C}$ , and is not recognizable at  $500\,^\circ\mathrm{C}$  (Figure S2). Therefore, we selected  $900\,^\circ\mathrm{C}$  as the pyrolysis temperature for all our materials. The BET surface area of as-pyrolyzed Co–C was measured to be  $197.6\,\mathrm{m^2\,g^{-1}}$ , higher than the  $115.4\,\mathrm{m^2\,g^{-1}}$  of as-pyrolyzed cotton C (Table S1). The higher surface area in the presence of Co may be due to decomposition of  $\mathrm{Co}(\mathrm{NO_3})_2$  during the

15213773, 2023, 30, Downloaded from https://onlinelibrary.wiley.com/doi/10.1002/anie.202305251 by University Of Pennsylvania, Wiley Online Library on [1903/2024]. See the Terms and Conditions (https://onlinelibrary.wiley.com/erms-and-conditions) on Wiley Online Library for rules of use; OA articles are governed by the applicable Creative Commons Licensea

pyrolysis which releases gas and creates extra pores in the carbon support structure. This is supported by the substantially increased pore volume with Co (Table S1). Co 2p core level X-ray photoelectron spectroscopy (XPS) can hardly detect any Co signal on the surface without sputtering (Figure S3), suggesting that the surface may be covered with carbon. The uniform dispersion of Co nanoparticles in the carbon matrix is a direct result of the chemical interaction between Co<sup>2+</sup> and the hydroxyl groups of cotton. As is known, natural cotton is a cellulose polymer with each glucose unit containing 3 hydroxyl groups, in theory accounting for 31.5 wt % of the material. [22] The abundant oxygen atoms can readily coordinate Co<sup>2+</sup>. If we pyrolyze cotton first to remove the hydroxyl groups and then follow the same procedure to load Co nanoparticles (sample named Co+C), aggregated Co particles with a broad size distribution are resulted (Figure S4).

Our pyrolyzed cotton substrates can efficiently convert light irradiation to heat. Under Xe lamp illumination with the power varied from 1.5 to 2.8 W cm $^{-2}$ , the surface temperature of as-pyrolyzed Co–C is constantly  $\approx\!50\,^{\circ}\text{C}$  higher than a carbon fiber paper substrate at each power density (Figure 2a and Figure S5a–c). Under 2.8 W cm $^{-2}$  illumination, the catalyst can reach a maximum surface temperature of  $\approx\!440\,^{\circ}\text{C}$  in 20 s (Figure 2b). Control experiments show

that the photothermal response is not influenced by the presence of the Co nanoparticles or their post-treatment/modification (Figure S6). Therefore, this high photothermal performance is an intrinsic property of the cotton-derived C substrate whose hierarchical porous structure enhances light absorption by trapping and scattering photons inside the bulk phase.<sup>[10]</sup>

Catalytic performance of as-pyrolyzed Co-C for photothermal CO<sub>2</sub> hydrogenation were tested without external heating in a flow reactor under 2.8 W cm<sup>-2</sup> illumination at the total pressure of 1 atm (Figure S5d). H<sub>2</sub> and CO<sub>2</sub> (1:1 by volume) were flowed at a total rate of 50 standard cubic centimeters per minute. CO and CH<sub>4</sub> were the only products detected. We consider CO to be a more valuable product than CH4 in this case because CO is a more important feedstock for the chemical industry and the reaction is endothermic ( $\Delta H = 41.2 \text{ kJ mol}^{-1}$ ) which can store solar energy. As-pyrolyzed Co-C shows a photothermal CO formation rate of 323 mmol  $g_{cat}^{-1} h^{-1}$  with a  $\approx 96 \%$  selectivity (Figure 2c). Increasing the Co loading in the catalyst improves the CO production rate but decreases the selectivity (Figure S7). By controlling the light intensity, we were able to adjust the temperature of the catalyst (Figure 2a and Figure S5e,f) and measure an activation energy of 64.8 kJ mol<sup>-1</sup> (Figure 2d) for the as-pyrolyzed Co-C

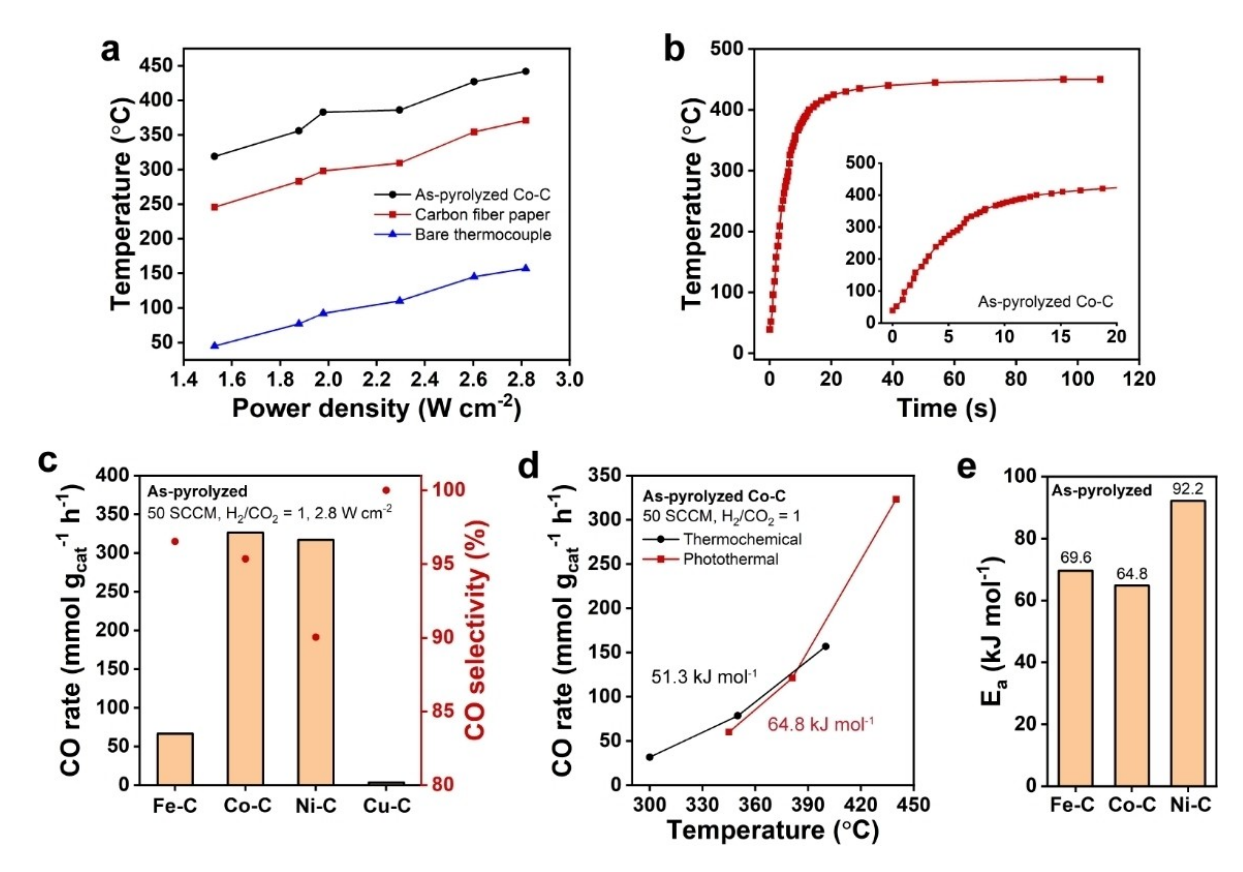


Figure 2. Study of photothermal response and kinetics in flow reactor. a) Stable temperature reached under illumination of varying power density, comparison between as-pyrolyzed Co–C and carbon fiber paper. b) Time response of temperature increase for as-pyrolyzed Co–C upon 2.8 W cm<sup>-2</sup> illumination. c) Photothermal  $CO_2$  hydrogenation reaction rate and product selectivity, comparison between as-pyrolyzed Fe–C, Co–C, Ni–C, and Cu–C catalysts. d) Temperature-dependent CO production rate and activation energy of as-pyrolyzed Co–C, comparison between thermochemical and photothermal reactions. e) Activation energy comparison of as-pyrolyzed Fe–C, Co–C, and Ni–C catalysts.

catalyst. To probe the nature of this photothermal reaction, we also studied the catalyst for thermochemical  $CO_2$  hydrogenation under identical reaction conditions but without light irradiation (Figure S5g). Similar reaction rates and activation energy (51.3 kJ mol $^{-1}$ ) to the photothermal reaction were observed (Figure 2d). This indicates that our photothermal  $CO_2$  hydrogenation reaction mainly proceeds via the thermochemical pathway instead of a photochemical pathway. [20]

We compared Fe, Co, Ni and Cu loaded on cotton-derived carbon for photothermal  $CO_2$  hydrogenation. The Fe–C, Ni–C and Cu–C catalysts were synthesized with the same method as Co–C and feature metallic phases with partially oxidized surfaces (Figure S8 and S9), resulting in similar photothermal conversion performance (Figure S10). Measured under identical reaction conditions as Co–C, Ni–C shows a similar CO formation rate but a lower selectivity than Co–C; Fe–C is significantly less active than Ni–C and Co–C; and Cu–C shows negligible activity (Figure 2c and Figure S11). These results corroborate that the catalytic activity of Co–C originates from Co instead of the carbon support. The photothermal activation energies of Fe–C, Co–C, and Ni–C are in the order of Ni>Co  $\approx$  Fe

(Figure 2e and Figure S12), a trend agreeing well with activation energies measured for the three metals in thermochemical  $\rm CO_2$  hydrogenation reactions. [23]

Treatment of as-pyrolyzed Co-C with H2 at 500°C for 30 min renders a porous structure as shown by SEM images featuring exposed nanoparticles after removing the surrounding matrix while still maintaining the carbon support (Figure 1c, Figure S13 and S14). Energy-dispersive X-ray (EDX) spectroscopy maps (Figure 1d) and XRD (Figure S15) confirm that the nanoparticles are cobalt metal, and the matrix is graphite. A Co  $2p_{3/2}$  XPS peak at 778.2 eV corresponding to Co(0) can be clearly observed after H<sub>2</sub> treatment (Figure S16), which might have removed the surface carbon and exposed the Co sites. If the cotton is pyrolyzed at temperatures lower than 900°C, H<sub>2</sub> treatment would remove most of the carbonaceous species which is insufficiently graphitized and leave a fragile and shrunken catalyst material (Figure S17). The structure of H<sub>2</sub>-activated Co-C catalyst resembles a lotus pod, where the Co nanoparticle lotus seeds are anchored in the porous carbon pod with their surroundings exposed (Figure 1e). Remarkably, the H<sub>2</sub>-activated catalyst increases the CO production rate to 650 mmol  $g_{cat}^{-1}h^{-1}$  with a  $\approx$  98 % selectivity (Figure 3a).

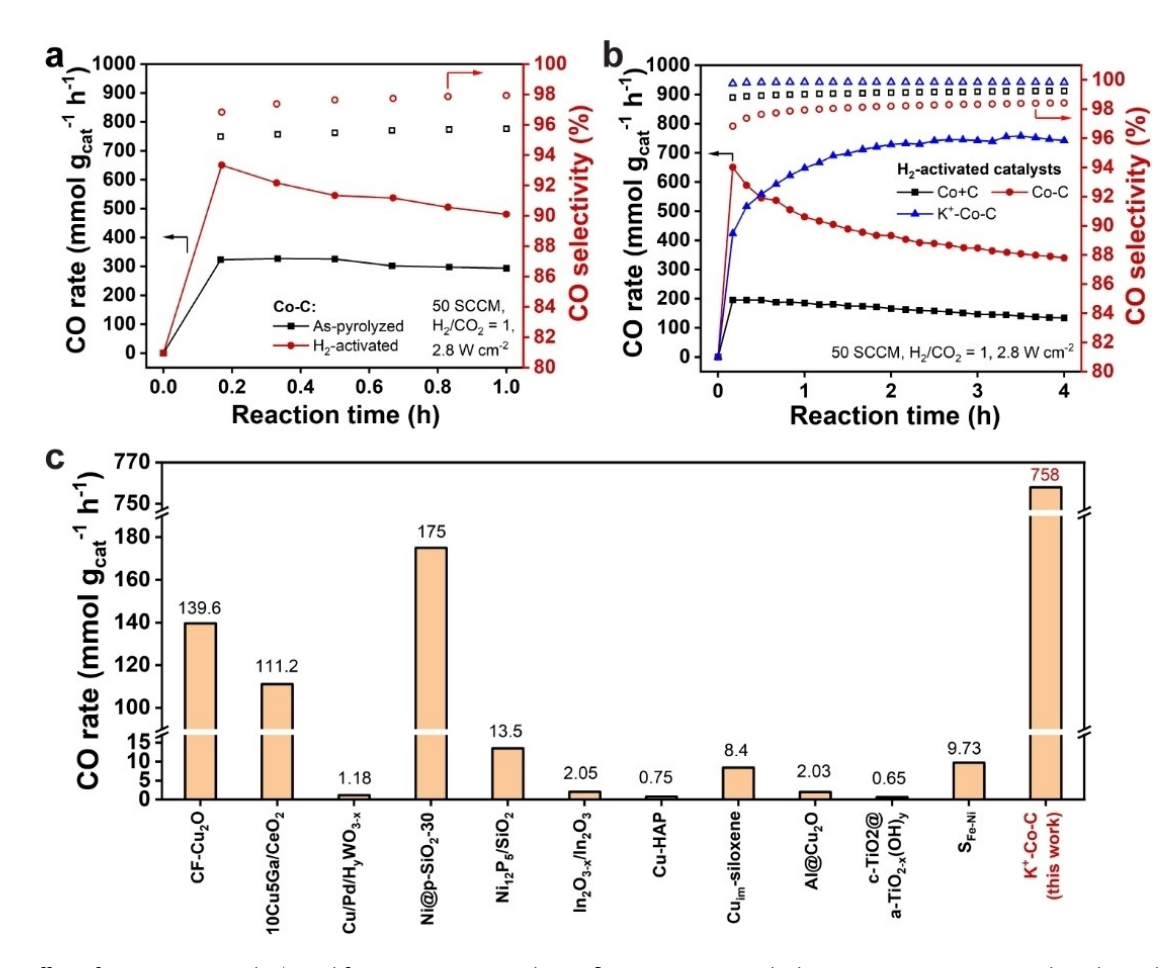


Figure 3. Effect of  $H_2$  treatment and  $K^+$  modification on Co–C catalyst in flow reactor. a)  $CO_2$  hydrogenation reaction rate and product selectivity, comparison between as-pyrolyzed and  $H_2$ -activated Co–C catalysts. b)  $CO_2$  hydrogenation reaction rate and product selectivity, comparison between  $H_2$ -activated Co+C, Co–C, and  $K^+$ -Co–C catalysts. c) Activity comparison of  $H_2$ -activated  $K^+$ -Co–C catalyst with other photothermal  $CO_2$  hydrogenation catalysts reported in the literature. Detailed reaction conditions are summarized in Table S3.

This reaction rate corresponds to 1477 mmol  $g_{\text{Co}}^{-1}h^{-1}$  based on Co mass and an estimated turnover frequency (TOF) of 2.39 s<sup>-1</sup>, approaching the highest reported mass activity of Co-based catalysts for photothermal CO<sub>2</sub> hydrogenation to CO (Table S2). <sup>[19]</sup> The measured activation energy is slightly lower but comparable to that of as-pyrolyzed Co–C (Figure S18), suggesting that H<sub>2</sub> activation mostly increase the active surface area of the catalyst rather than alter the nature of the catalytic site. In contrast, the Co+C catalyst (Figure S19) shows a low CO rate of 195 mmol  $g_{\text{cat}}^{-1}h^{-1}$  even after H<sub>2</sub> activation (Figure 3b, black), demonstrating the importance of high Co dispersion and intimate Co/C interfaces for high catalytic activity.

The CO production rate of H<sub>2</sub>-activated Co–C gradually decreases to  $\approx 50\%$  of the initial value after 4 h (Figure 3b, red), which may be due to CO poisoning the Co sites. [24] To address this issue, we modified Co-C with K+ which is known to lower the CO binding energy. [25-27] The K+-Co-C catalyst was prepared by drop-casting KNO3 into aspyrolyzed Co-C and then treating it in H<sub>2</sub> at 500 °C. Increasing the added amount of KNO3 from 0.2 wt % the mass of as-pyrolyzed Co-C to 10 wt % improves CO selectivity while retaining the production rate, whereas further increasing it to 30 wt % does not change the selectivity or activity (Figure S20). Therefore, we selected 10 wt % as the optimal amount for our study. K<sup>+</sup>-Co-C exhibits a lotus-pod structure similar to Co-C with a homogeneous distribution of the K element (Figure 1g and Figure S21a). The pores and Co particles in K<sup>+</sup>-Co-C show similar size distributions centered around 120 nm (Figure S22), analogous to the lotus-pod structure where seeds reside in pores with matched sizes (Figure 1e). K<sup>+</sup>-Co-C exhibits a BET surface area of 194.5 m<sup>2</sup> g<sup>-1</sup>, similar to aspyrolyzed Co-C, and a considerably higher pore volume (Table S1). High-angle annular dark field scanning transmission electron microscopy (HAADF-STEM) shows crystalline Co nanoparticles with expected lattice fringes attached to porous carbon (Figure 1f). K<sup>+</sup>-Co-C shows almost the same XRD pattern (Figure S23) and Co 2p XPS

binding energy (Figure S24) as Co-C, demonstrating that K<sup>+</sup> modification does not change the bulk phase or surface oxidation state of Co. Under identical photothermal CO<sub>2</sub> hydrogenation conditions, our K+-Co-C catalyst shows a stable CO formation rate of 758 mmol g<sub>cat</sub><sup>-1</sup>h<sup>-1</sup> with a 99.8 % selectivity (Figure 3b blue). This CO rate is at least 4 times higher than other CO<sub>2</sub> hydrogenation catalysts tested under similar conditions (Figure 3c and Table S3).[13-16,18,20,28-32] When normalized to the mass of Co, the CO production rate is  $2871 \text{ mmol g}_{Co}^{-1} h^{-1}$  with an estimated TOF of  $4.65 \text{ s}^{-1}$ , superior to all other Co-based photothermal CO2 hydrogenation catalysts reported to date (Table S2).[19,21,33-38] K<sup>+</sup> -Co-C synthesized from KNO<sub>3</sub> and KCl show similar CO productivity and selectivity, demonstrating that the performance improvement is indeed caused by K<sup>+</sup>. Na<sup>+</sup> addition can also improve CO selectivity, but to a less extent than K<sup>+</sup> (Figure S25). The catalyst's morphology (Figure S21b), elemental distribution (Figure S21c), and crystal structure (Figure S23) remain unchanged after 8 hours on stream. Notably, K<sup>+</sup> modification increases the activation energy substantially from 54.3 kJ mol<sup>-1</sup> to 90.0 kJ mol<sup>-1</sup> (Figure S18). This is likely due to suppressed H<sub>2</sub> adsorption, <sup>[25–27]</sup> which is also responsible for the improved selectivity for CO (as opposed to further hydrogenated CH<sub>4</sub>). Compared with other catalysts, [14,18,20,29] the superior performance of K+ -Co-C likely originates from its improved photothermal conversion efficiency and increased exposure of Co sites.

To realize higher  $CO_2$  conversion, we investigated photothermal  $CO_2$  hydrogenation in a batch reactor (Figure S5c). Under 2.8 W cm<sup>-2</sup> illumination (catalyst surface temperature  $\approx 440\,^{\circ}\text{C}$ ) with 1:1 H<sub>2</sub>/CO<sub>2</sub> (by volume) at a total pressure of 1 atm, the H<sub>2</sub>-activated Co–C catalyst achieves a  $CO_2$  conversion of  $\approx 25\,\%$  after 30 min, approaching the thermodynamic equilibrium value of 28.4 % (Figure 4a and Figure S26). However, the selectivity for CO is below 80 % due to CH<sub>4</sub> formation. This decrease in selectivity is associated with CO accumulation in the batch reactor during the reaction which leads to further hydrogenation of CO to  $CH_4$  (Figure S27). [10] Remarkably, the K<sup>+</sup>

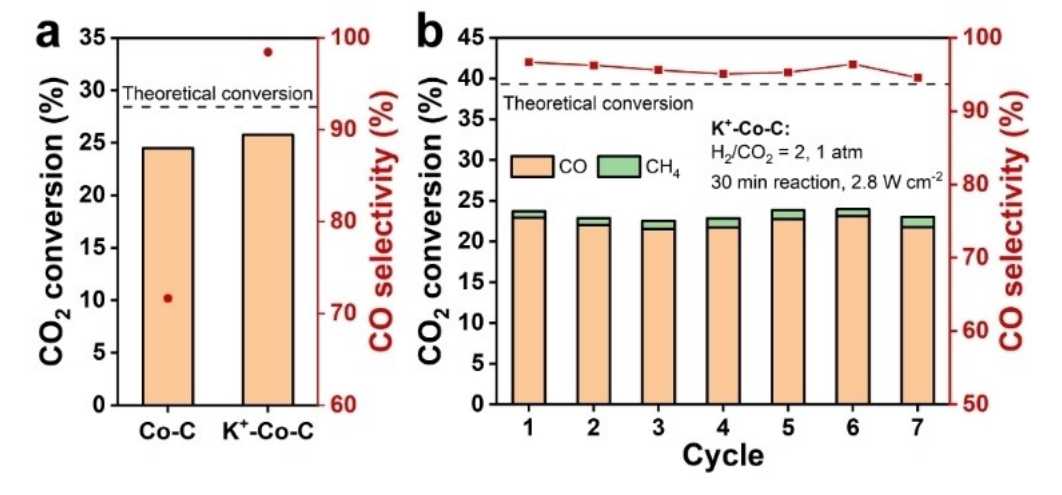


Figure 4. Study of CO<sub>2</sub> conversion in batch reactor. a) Catalytic performance of H<sub>2</sub>-activated Co–C and K<sup>+</sup>–Co–C in a batch reactor with 1:1 H<sub>2</sub>/CO<sub>2</sub> for 30 min. b) Cycling stability of H<sub>2</sub>-activated K<sup>+</sup>–Co–C.

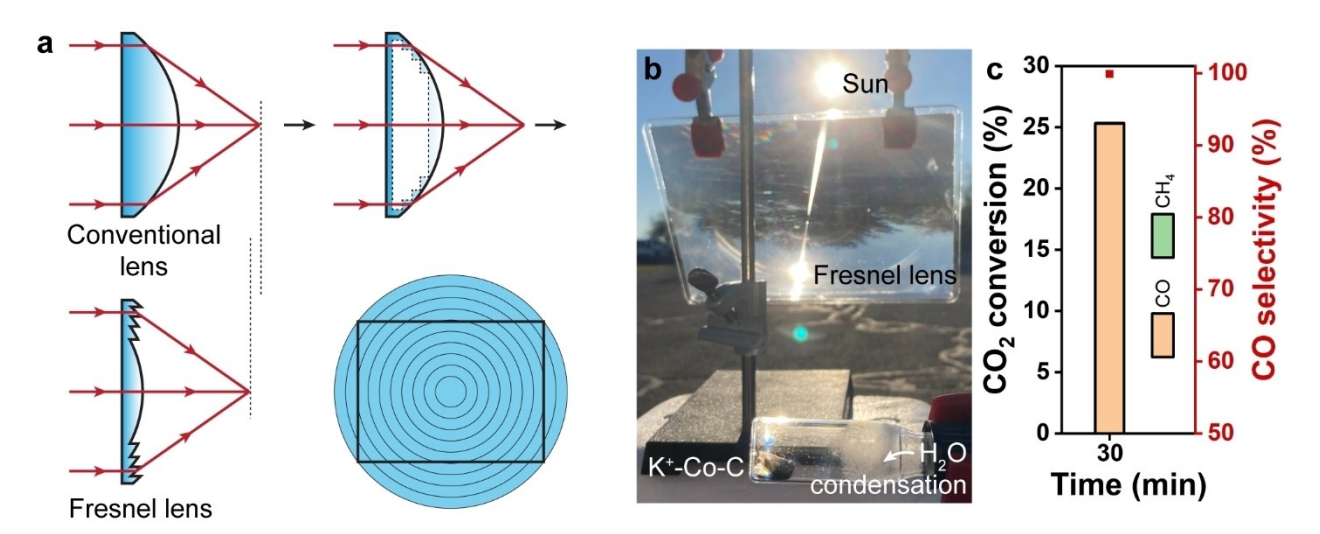


Figure 5. Demonstration of  $CO_2$  hydrogenation in batch reactor under natural sunlight concentrated by a plastic Fresnel lens. a) Comparison between conventional lens and Fresnel lens. b) Experimental setup. c) Conversion and product distribution after 30 min of reaction (1:1  $H_2/CO_2$ ).

-Co-C catalyst still maintains a high CO selectivity of > 95 % while achieving a high CO<sub>2</sub> conversion of  $\approx$  25 % (Figure 4a), benefited from the  $K^+$  modification suppressing CO and H<sub>2</sub> adsorption. [25-27] The simultaneously high CO<sub>2</sub> conversion and CO selectivity of K+-Co-C motivated us to pursue even higher CO<sub>2</sub> conversion by increasing the H<sub>2</sub>/ CO<sub>2</sub> ratio. Unfortunately, CO<sub>2</sub> conversion was not effectively improved because increasing the H<sub>2</sub>/CO<sub>2</sub> ratio leads to decreased CO<sub>2</sub> partial pressure (the total pressure is kept at 1 atm) which in turn decreases the reaction rate. At H<sub>2</sub>/CO<sub>2</sub> ratios >3, the reaction was unable to reach equilibrium within the  $\approx 100 \, \text{min}$  reaction time and therefore the observed conversion is low (Figure S28). At a H<sub>2</sub>/CO<sub>2</sub> volume ratio of 2, H<sub>2</sub>-activated K<sup>+</sup>-Co-C retains > 22 % CO<sub>2</sub> conversion and >95% CO selectivity for at least 7 consecutive batch reaction cycles, reflecting good durability of the catalyst (Figure 4b).

The high performance of the H<sub>2</sub>-activated K<sup>+</sup>-Co-C catalyst enabled us to drive photothermal CO<sub>2</sub> hydrogenation under natural sunlight utilizing a plastic Fresnel lens as a cost-effective solar concentrator (Figure 5a). Compared to the conventional lens, the Fresnel lens retains the refracting surface while removing some of the inner material, resulting in a reduced thickness and a shorter focal length. [39] The low thickness reduces light absorption by the lens itself and thus enables its manufacturing with cost-effective materials such as plastics. We utilized a 32.5 × 23.6 cm<sup>2</sup> plastic Fresnel lens to focus sunlight onto our  $1 \times 1$  cm<sup>2</sup> sized catalyst, resulting in a temperature increase from 12°C to 585°C during the winter season at 1 h before sunset (Figure 5b). After a 30 min batch reaction with 1:1 H<sub>2</sub>/CO<sub>2</sub>, K<sup>+</sup>-Co-C shows 25%  $CO_2$  conversion with  $\approx 100$ % CO selectivity (Figure 5c). At sunset, the temperature on the catalyst surface gradually decreases from 473 °C to 11 °C, and K+-Co-C still retains  $\approx 6\%$  CO<sub>2</sub> conversion with  $\approx 100\%$  CO selectivity (Figure S29).

In summary, we have developed a lotus-pod-structured  $K^+$ -Co-C catalyst with record-high activity and near-unity

CO selectivity for the photothermal CO<sub>2</sub> hydrogenation reaction. The high performance is rendered by efficient heat transfer through the intimate Co/C interface, exposed Co catalytic sites, and facilitated heat generation and mass transport within the hierarchical porous carbon matrix. This work demonstrates photothermal catalyst design for solar fuel production and CO<sub>2</sub> utilization.

### **Acknowledgements**

This work was solely supported by the Center for Hybrid Approaches in Solar Energy to Liquid Fuels (CHASE), an Energy Innovation Hub funded by the U.S. Department of Energy, Office of Science, Office of Basic Energy Sciences under Award Number DE-SC0021173. The electron microscopy was carried out at the Singh Center for Nanotechnology, which is supported by the NSF National Nanotechnology Coordinated Infrastructure Program under grant NNCI-2025608. Additional support to the Nanoscale Characterization Facility at the Singh Center has been provided by the Laboratory for Research on the Structure of Matter (MRSEC) supported by the National Science Foundation (DMR-1720530).

#### **Conflict of Interest**

The authors declare no conflict of interest.

#### **Data Availability Statement**

The data that support the findings of this study are available from the corresponding author upon reasonable request.

5213773, 2023, 30, Downloaded from https://onlinelibrary.wiley.com/doi/10.1002/anie.202305251 by University Of Pennsylvania, Wiley Online Library on [1903/2024]. See the Terms and Conditions (https://onlinelibrary.wiley.com/terms-and-conditions) on Wiley Online Library for rules of use; OA articles are governed by the applicable Cerative Commons License



5213773, 2023,

, 30, Downloaded from https://onlinelibrary.wiley.com/doi/10.1002/anie.202305251 by University Of Pennsylvania, Wiley Online Library on [19/03/2024]. See the Terms and Conditions (https://onlinelibrary.wiley.com/rerms-and-conditions) on Wiley Online Library for rules of use; OA articles are governed by the applicable Creative Commons

**Keywords:** CO<sub>2</sub> Hydrogenation · Hybrid Material · Photothermal Catalysis · Reverse Water-Gas Shift · Solar Fuel

- [1] S. J. Davis, N. S. Lewis, M. Shaner, S. Aggarwal, D. Arent, I. L. Azevedo, S. M. Benson, T. Bradley, J. Brouwer, Y. M. Chiang, C. T. M. Clack, A. Cohen, S. Doig, J. Edmonds, P. Fennell, C. B. Field, B. Hannegan, B. M. Hodge, M. I. Hoffert, E. Ingersoll, P. Jaramillo, K. S. Lackner, K. J. Mach, M. Mastrandrea, J. Ogden, P. F. Peterson, D. L. Sanchez, D. Sperling, J. Stagner, J. E. Trancik, C. J. Yang, K. Caldeira, Science 2018, 360, 1419–1427.
- [2] Y. Dong, P. Duchesne, A. Mohan, K. K. Ghuman, P. Kant, L. Hurtado, U. Ulmer, J. Y. Y. Loh, A. A. Tountas, L. Wang, A. Jelle, M. Xia, R. Dittmeyer, G. A. Ozin, *Chem. Soc. Rev.* 2020, 49, 5648–5663.
- [3] J. Fu, K. Jiang, X. Qiu, J. Yu, M. Liu, Mater. Today 2020, 32, 222–243.
- [4] S. Yao, J. He, F. Gao, H. Wang, J. Lin, Y. Bai, J. Fang, F. Zhu, F. Huang, M. Wang, J. Mater. Chem. A 2023, 10.1039/D2TA09234D.
- [5] G. Zhang, Z. Wang, J. Wu, Nanoscale 2021, 13, 4359–4389.
- [6] Y. Zhang, B. Xia, J. Ran, K. Davey, S. Z. Qiao, Adv. Energy Mater. 2020, 10, 1903879.
- [7] E. Fujita, D. C. Grills, G. F. Manbeck, D. E. Polyansky, Acc. Chem. Res. 2022, 55, 616–628.
- [8] Z. Wang, Z. Yang, Z. C. Kadirova, M. Guo, R. Fang, J. He, Y. Yan, J. Ran, Coord. Chem. Rev. 2022, 473, 214794–214830.
- [9] H. Liu, L. Shi, Q. Zhang, P. Qi, Y. Zhao, Q. Meng, X. Feng, H. Wang, J. Ye, Chem. Commun. 2021, 57, 1279–1294.
- [10] M. Ghoussoub, M. Xia, P. N. Duchesne, D. Segal, G. Ozin, Energy Environ. Sci. 2019, 12, 1122–1142.
- [11] M. González-Castaño, B. Dorneanu, H. Arellano-García, React. Chem. Eng. 2021, 6, 954–976.
- [12] M. Jörges, F. Krischer, V. H. Gessner, Science 2022, 378, 1331– 1336
- [13] Y. F. Xu, P. N. Duchesne, L. Wang, A. Tavasoli, A. A. Jelle, M. Xia, J. F. Liao, D. B. Kuang, G. A. Ozin, *Nat. Commun.* 2020, 11, 5149.
- [14] J. Guo, P. N. Duchesne, L. Wang, R. Song, M. Xia, U. Ulmer, W. Sun, Y. Dong, J. Y. Y. Loh, N. P. Kherani, J. Du, B. Zhu, W. Huang, S. Zhang, G. A. Ozin, ACS Catal. 2020, 10, 13668– 13681
- [15] M. Cai, Z. Wu, Z. Li, L. Wang, W. Sun, A. A. Tountas, C. Li, S. Wang, K. Feng, A.-B. Xu, S. Tang, A. Tavasoli, M. Peng, W. Liu, A. S. Helmy, L. He, G. A. Ozin, X. Zhang, *Nat. Energy* 2021, 6, 807–814.
- [16] H. Robatjazi, H. Zhao, D. F. Swearer, N. J. Hogan, L. Zhou, A. Alabastri, M. J. McClain, P. Nordlander, N. J. Halas, *Nat. Commun.* 2017, 8, 27.
- [17] Y. Li, Z. Zeng, Y. Zhang, Y. Chen, W. Wang, X. Xu, M. Du, Z. Li, Z. Zou, ACS Sustainable Chem. Eng. 2022, 10, 6382– 6388.
- [18] B. Deng, H. Song, K. Peng, Q. Li, J. Ye, Appl. Catal. B 2021, 298, 120519–120528.
- [19] X. Shen, C. Li, Z. Wu, R. Tang, J. Shen, M. Chu, A. B. Xu, B. Zhang, L. He, X. Zhang, *Nanoscale* 2022, 14, 11568–11574.

- [20] S. Wang, D. Zhang, W. Wang, J. Zhong, K. Feng, Z. Wu, B. Du, J. He, Z. Li, L. He, W. Sun, D. Yang, G. A. Ozin, *Nat. Commun.* 2022, 13, 5305.
- [21] S. Ning, H. Xu, Y. Qi, L. Song, Q. Zhang, S. Ouyang, J. Ye, ACS Catal. 2020, 10, 4726–4736.
- [22] J. Qian, Q. Dong, K. Chun, D. Zhu, X. Zhang, Y. Mao, J. N. Culver, S. Tai, J. R. German, D. P. Dean, J. T. Miller, L. Wang, T. Wu, T. Li, A. H. Brozena, R. M. Briber, D. K. Milton, W. E. Bentley, L. Hu, *Nat. Nanotechnol.* 2023, 18, 168–176.
- [23] T. Osaki, N. Narita, T. Horiuchi, T. Sugiyama, H. Masuda, K. Suzuki, J. Mol. Catal. A 1997, 125, 63–71.
- [24] S. Vijay, W. Ju, S. Brückner, S.-C. Tsang, P. Strasser, K. Chan, Nat. Catal. 2021, 4, 1024–1031.
- [25] S. Li, Y. Xu, H. Wang, B. Teng, Q. Liu, Q. Li, L. Xu, X. Liu, J. Lu, Angew. Chem. Int. Ed. 2023, 62, e202218167.
- [26] J. Xu, X. Gong, R. Hu, Z.-w. Liu, Z.-t. Liu, J. Mol. Catal. 2021, 516, 111954–111964.
- [27] X. Yang, X. Su, X. Chen, H. Duan, B. Liang, Q. Liu, X. Liu, Y. Ren, Y. Huang, T. Zhang, *Appl. Catal. B* **2017**, *216*, 95–105.
- [28] Y. F. Li, W. Lu, K. Chen, P. Duchesne, A. Jelle, M. Xia, T. E. Wood, U. Ulmer, G. A. Ozin, J. Am. Chem. Soc. 2019, 141, 14991–14996.
- [29] Z. Li, C. Mao, Q. Pei, P. N. Duchesne, T. He, M. Xia, J. Wang, L. Wang, R. Song, A. A. Jelle, D. M. Meira, Q. Ge, K. K. Ghuman, L. He, X. Zhang, G. A. Ozin, *Nat. Commun.* 2022, 13, 7205.
- [30] Y. Su, S. Wang, L. Ji, C. Zhang, H. Cai, H. Zhang, W. Sun, Nanoscale 2023, 15, 154–161.
- [31] L. Wan, Q. Zhou, X. Wang, T. E. Wood, L. Wang, P. N. Duchesne, J. Guo, X. Yan, M. Xia, Y. F. Li, A. A. Jelle, U. Ulmer, J. Jia, T. Li, W. Sun, G. A. Ozin, *Nat. Catal.* 2019, 2, 889–898.
- [32] L. Wang, Y. Dong, T. Yan, Z. Hu, A. A. Jelle, D. M. Meira, P. N. Duchesne, J. Y. Y. Loh, C. Qiu, E. E. Storey, Y. Xu, W. Sun, M. Ghoussoub, N. P. Kherani, A. S. Helmy, G. A. Ozin, Nat. Commun. 2020, 11, 2432.
- [33] X. Meng, T. Wang, L. Liu, S. Ouyang, P. Li, H. Hu, T. Kako, H. Iwai, A. Tanaka, J. Ye, Angew. Chem. Int. Ed. 2014, 53, 11478–11482.
- [34] Y. Fang, K. Lv, Z. Li, N. Kong, S. Wang, A. B. Xu, Z. Wu, F. Jiang, C. Li, G. A. Ozin, L. He, Adv. Sci. 2020, 7, 2000310.
- [35] K. Feng, S. Wang, D. Zhang, L. Wang, Y. Yu, K. Feng, Z. Li, Z. Zhu, C. Li, M. Cai, Z. Wu, N. Kong, B. Yan, J. Zhong, X. Zhang, G. A. Ozin, L. He, Adv. Mater. 2020, 32, 2000014.
- [36] D. Zhang, K. Lv, C. Li, Y. Fang, S. Wang, Z. Chen, Z. Wu, W. Guan, D. Lou, W. Sun, D. Yang, L. He, X. Zhang, Sol. RRL 2021. 5, 2000387.
- [37] D. Lou, A. B. Xu, Y. Fang, M. Cai, K. Lv, D. Zhang, X. Wang, Y. Huang, C. Li, L. He, *ChemNanoMat* 2021, 7, 1008–1012.
- [38] L. He, C. Li, M. Xiao, Z. Chen, C. Zhang, Z. Wu, Z. Zhu, X. Wang, J. Inorg. Mater. 2022, 37, 22–28.
- [39] W. T. Xie, Y. J. Dai, R. Z. Wang, K. Sumathy, Renewable Sustainable Energy Rev. 2011, 15, 2588–2606.

Manuscript received: April 13, 2023 Accepted manuscript online: May 26, 2023 Version of record online: June 14, 2023